Modeling of tribo-electrification of a pneumatically conveyed powder in a squared duct using DEM-CFD.

M.W. Korevaar[*‡], J.T. Padding[‡], M.A. Van der Hoef[§], J.A.M. Kuipers[‡]

[‡] Dept. of Chemical Engineering
Eindhoven University of Technology
[*] Corresponding author:
m.w.korevaar@tue.nl

[§] Dept. of Science and Technology
University of Twente

Abstract – **Dry separation technology is a sustainable alternative to conventional wet separation technology for production of food ingredients. This paper is concerned with the exploration of a new driving force for dry separation, i.e. tribo-electrification.**

To investigate the possibilities of this driving force, we modified our in-house DEM-CFD code to model a learning system where powder is tribo-electrically charged by conveying it pneumatically through a squared tube. The charged particles will electrostatically interact with both other charged particles, as well as their induced charges on the conducting walls.

We show that the amount of acquired charge depends on the electrostatic interaction between particles and walls and show the corresponding spatial distribution of the particles. They depend both highly on the (mean) charge of the particles. We observed a critical charge per particle after which particles charged rapidly to their saturation charge. This critical charge is delicate and lower than expected from first order derivations.

I. INTRODUCTION

With the increasing world population and the limited availability of resources on our planet, our food production system needs to become more efficient. Nowadays, food ingredient isolation via wet processing requires huge amounts of water and energy. An alternative approach towards extraction of food ingredients is dry separation technology, in which milled raw materials are fractionated on the basis of their composition into enriched ingredient fractions [1], [2]. Dry-fractionation relies on separation technologies such as air-classification, sieving and electrostatic separation, where the latter needs a charging mechanism like tribo-electrification; the exchange of charge when two bodies of different material make contact. This happens e.g. when combing your hair. Because different materials charge differently this phenomenon can be used for separation which is already applied in the mining industry and also for waste separation (even if it consists only of dielectric material) [3].

The phenomenon of tribo-electrification was already described in ancient Greece. However, current knowledge of the underlying mechanism is still very limited. It is for example unknown whether charge transfer is caused by electrons, ions, the exchange of material or a combination of these mechanisms. This and more on tribo-electrification is described in the review by Matsusaka et al. [4].

Classical theory explains the tribo-electrification of metals using their work functions; two materials with different work function need different amounts of energy to knock an electron out. When these materials touch, there will be a net flow of electrons from the lower work function to the higher work function until the Fermi levels are equal. As this is an electron-based charge transfer, it can only explain part of the experiments. As a matter of fact, this theory is not applicable for metal-insulator contact, because insulators do not have free electrons available. Therefore, effective work functions have been proposed for insulators to describe some of the experiments

However, Matsuyama et al. showed that for insulator spheres impacting on a metal plate, the transfered charge is independent of the work function of the metal [5], [6]. They found a stronger dependence on the dielectric constant of the non-metal and hypothesize that the particle's acquired charge is limited by the relaxation of charge due to air-breakdown.

Particle based modeling of the tribo-electrification of moving particles has had some attention in literature. With the increase of computational power it is now possible to model the trajectory of each individual particle, using the so-called Discrete Element Model (DEM). On top of that, the dynamics of the surrounding fluid phase can be studied using Computational Fluid Dynamics (CFD) approaches. The particle and fluid dynamics can be solved in a coupled fashion which is referred to as DEM-CFD or Discrete Particle Modeling (DPM).

Tanoue et al. used the DEM-CFD framework to model powder pneumatically conveyed through a tube [7]. They used a limited number of particles (1000) in a 2D cylindrical coordinate system using $\kappa - \varepsilon$ turbulence modeling. They compared their simulation results to experimental results. A good agreement was found for the relation between particle diameter and acquired charge. The relation between acquired charge and gas velocity / tube diameter however, was in disagreement. They suggested that the denser flow and longer tube of the experiments, increased the influence of space charge and image charges. As these were not included in the model, this may explain its incorrect trends.

Hogue et al. [8] did experiments and DEM simulation on particles rolling down a chute. They included electrostatic particle interactions, but neglected the charge on the chute, which is either the image charge in case of a metal chute, or the residual charge in case of an isolating chute. The latter was added in a follow up paper [9]. They introduced a screening of the electrostatic forces as also found in the calculation of the potential in an electrolyte solution. Addition of this screening term increased the similarity between experiments and simulations in terms of interparticle distance.

Finally, Matsuyama et al. [10] performed DEM simulations where particles were shaken in a bud which were directly compared to an similar experimental setup. In this setup they were able to measure the charge on a single particle which served as input for their multi-

particle (approximately 230) simulation. Their simulations represented the trends from the experiments, while being an factor two too high in determining the acquired charge. They did not take into account the actual contact area of a collision but rather the fact that the time integrated contact area will increase in time. They included image charge and space charge effects which improved the resemblance of simulation and experiments, but were unclear on how it was implemented or influenced the results.

In the work mentioned above, a generally applied model for the acquired charge of a particle Δq, is

$$\Delta q = a \left(1 - \frac{q_{in}}{q_{sat}} \right). \tag{1}$$

where a is some constant that needs to be determined experimentally, q_{in} is the charge on the particle and q_{sat} is the saturation charge of the particle which is either estimated or also determined experimentally. Only Matsuyama et al. determined these parameters as lumped parameters from *single* particle experiments, while only Tanoue et al.[7] let α explicitly depend on the contact area. Note that the acquired charge can be calculated per unit time, per unit of rolling/sliding distance or per collision.

The simple model of Eq. (1) is inspired by the (abundant) experimental observations that the charge goes to a saturation charge in an exponential fashion which is generally explained by the condenser model. In that case, two touching particles are considered as two parallel plates at the contact area, thus a capacitor. The difference in work function is then the driving force to charge this capacitor. However, as mentioned before, the work functions are not suitable or sufficient to describe the charging, especially when particle detaches from the wall, after getting charged. Ireland et al. [11] suggested to treat the contribution of different contact modes differently. They distinguished between rolling, sliding and bouncing. For rolling and sliding they suggested a condenser like model, while for bouncing they used the air-break down model. Including the latter limited the charge built up at the particles which turned out to be more in agreement with their experiments.

The main goal of our project is to model a charging device for food products. However, because current knowledge of tribo-electrification in such devices is limited, it is not yet possible to develop a fully predictive model. First we need to rely on a learning model to acquire a better understanding of such systems.

We will therefore extent a sophisticated Discrete Element Model (DEM) by incorporating all relevant physical factors. This includes the coupling with the gas phase which is solved by Computational Fluid Dynamics (CFD) as well as electrostatic forces. In this paper we will focus on the role of the interparticle electrostatic forces. Reason to do so is that other researchers neglect this force as it is deemed too small, or authors are not clear on the influence of this force. This also includes the force from the induced charge on the walls, because the walls will be constructed from metal in the final application we envision. We will show that induced charges can play an significant role in the spatial distribution of particles, as well as their acquired charge.

TABLE I – Boundary conditions for the flow solver.

boundary	boundary condition	description
Entrance ($z = 0$)	$\vec{v}_g(x,y) = \frac{16\beta^2}{\pi^4} \sum\limits_{n,m \text{ odd}}^{\infty} \frac{\sin(n\pi x/a)\sin(m\pi y/b)}{nm(\beta^2 n^2 + m^2)} \vec{e}_z$	Prescribed flow profile.
Walls	$v_{g,x} = v_{g,y} = v_{g,z} = 0$	No-slip, impermeable wall.
Exit ($z = L_z$)	$\frac{\partial}{\partial z}\vec{v}_g = 0$	Developed flow.
	$p = p_0$	Prescribed pressure.

II. METHODS

A. DEM-CFD

For the simulations in this work, we have made use of an in-house code of DEM-CFD model. Details of this code have been extensively explained in previous works, e.g. [12]. The main features of the model are explained below.

To describe the flow field of our multi-phase (gas-solid) flow, a modified Navier-Stokes equation [13] needs to be solved. The influence of the solid on the gas is accounted for by including the gas volume fraction ε and a source term $\vec{S}_{f\to p}$ to account for the inter-phase drag:

$$\rho_g \frac{\partial \varepsilon}{\partial t} + \rho_g \nabla \cdot (\varepsilon \vec{v}_g) = 0, \tag{2}$$

$$\rho_g \frac{\partial (\varepsilon \vec{v}_g)}{\partial t} + \rho_g \nabla \cdot (\varepsilon \vec{v}_g \vec{v}_g) = -\varepsilon \nabla p - \nabla \cdot \left(\varepsilon \mu_g \left((\nabla \vec{v}_g) + (\nabla \vec{v}_g)^T \right) \right) - \vec{S}_{f\to p} + \varepsilon \rho_g \vec{g}. \tag{3}$$

Here ρ_g is the density, u_g the velocity vector, p the pressure, μ the viscosity and g the gravity. The inter-phase drag is calculated by mapping the drag from the particles Eq. (7) to their eight closest nodes of the computational cells. These equations are solved numerically using a semi-implicit, first order finite difference scheme. The domain is defined in Fig. 1 and the necessary boundary conditions are given in Table I.

No sub-grid turbulence model has been applied because the simulations are performed under laminar flow conditions with a Reynolds number around 1100.

The solid phase is solved by calculating the trajectories of all particles individually. This is done by solving Newtons second law for translation and rotation

$$m_p \vec{a} = \vec{F}_g + \vec{F}_{elec} + \vec{F}_D + \vec{F}_{\nabla p} + \vec{F}_c$$
$$I \frac{\partial \vec{\omega}}{\partial t} = \vec{T}. \tag{4}$$

Here m_p is the particle mass, $\vec{a}$ its acceleration, I its moment of inertia and ω the angular velocity. Furthermore, $\vec{F}$ represents the different forces and $\vec{T}$ the torque; they are both defined in Table II. Note that the contact forces are calculated using a soft sphere model with a linear spring-dashpot [14], [15]. Equation (4) is solved using a simple explicit integration scheme.

TABLE II – Overview of implemented forces. The symbols are defined in Table IV.

Gravity

$$\vec{F}_g = m_p \, g \vec{e}_z \tag{5}$$

Bouyance force

$$\vec{F}_{\nabla p} = -V_p \nabla p \tag{6}$$

Drag force

$$\vec{F}_D = \frac{V_p \, \beta}{1 - \varepsilon} \left(\vec{v}_g - \vec{v}_p \right) \tag{7}$$

$$\beta = \begin{cases} 150 \dfrac{(1 - \varepsilon)^2 \, \mu_g}{\varepsilon D_p^2} + 1.75 \, (1 - \varepsilon) \, \dfrac{\rho_g}{D_p} \| \vec{v}_g - \vec{v}_p \| & \text{for} \quad \varepsilon < 0.80 \\ \frac{3}{4} \, C_D \dfrac{\varepsilon \, (1 - \varepsilon)}{D_p} \rho_g \| \vec{v}_g - \vec{v}_p \| \varepsilon^{-2.65} & \text{for} \quad \varepsilon > 0.80 \end{cases} \tag{8}$$

with

$$C_D = \begin{cases} \dfrac{24}{Re_p} \left(1 + 0.15 \, Re_p^{0.687} \right) & \text{for} \quad Re_p < 1000 \\ 0.44 & \text{for} \quad Re_p \leq 1000 \end{cases} \tag{9}$$

$$Re_p = \frac{\varepsilon \, \rho_g \| \vec{v}_g - \vec{v}_p \| D_p}{\mu_g} \tag{10}$$

Contact forces

$$\vec{F}_{c,i} = \sum_{j=1}^{N_c} \left(\vec{F}_{n,ij} + \vec{F}_{t,ij} \right) \tag{11}$$

$$\vec{F}_{n,ij} = -k_n \delta_n \vec{e}_n - \eta_n (\vec{v}_{p,i} - \vec{v}_{p,j}) \cdot \vec{e}_n \tag{12}$$

$$\vec{F}_{t,ij} = \begin{cases} -k_t \delta_t \vec{e}_t - \eta_t (\vec{v}_{p,i} - \vec{v}_{p,j}) \cdot \vec{e}_t & \text{if} \quad \| F_{t,ij} \| \leq \mu \| F_{n,ij} \| \\ -\mu \| F_{n,ij} \| \vec{e}_t & \text{if} \quad \| F_{t,ij} \| > \mu \| F_{n,ij} \| \end{cases} \tag{13}$$

$$\eta_n = \frac{-2 \ln e_n \sqrt{m_{eff} k_n}}{\sqrt{\pi^2 + \ln^2 e_n}}, \quad \eta_t = \frac{-2 \ln e_t \sqrt{2/7 m_{eff} k_t}}{\sqrt{\pi^2 + \ln^2 e_t}} \tag{14}$$

$$\vec{T}_i = \sum_{j=1}^{N_c} \left(R_{p,ij} \times F_{t,ij} \vec{e}_t \right), \quad 1/m_{eff} = 1/m_i + 1/m_j \tag{15}$$

Electric forces

$$\vec{F}_{el,i} = -q_i \, \nabla_i \Phi_i \tag{16}$$

$$\Phi_i = \sum_{j=1}^{N_p} \frac{q_j}{4\pi\varepsilon_0} \times \begin{cases} \displaystyle\sum_{n=-N_{im}}^{N_{im}} {}' \left(A_{ij,n}^- - A_{ij,n}^+ \right) + \xi_{ij,N_{im}} & \text{for} \quad z_{ij} \leq z_{ff} \\ \dfrac{2}{L_y} \sqrt{\dfrac{8}{r_{ij} L_y}} \cos\left(\dfrac{\pi y_i}{L_y} \right) \cos\left(\dfrac{\pi y_j}{L_y} \right) e^{-\dfrac{\pi r_{ij}}{L_y}} & \text{for} \quad z_{ff} < z_{ij} \leq z_c \\ 0 & \text{for} \quad z_{ij} > z_c \end{cases} \tag{17}$$

where $\sum'$ indicates that the term $n = 0$ is omitted if $i = j$,

$$A_{ij,n}^- = \left(r_{ij}^2 + (y_i - y_j + 2n L_y)^2 \right)^{-1/2}, \quad A_{ij,n}^+ = \left(r_{ij}^2 + (y_i + y_j + (2n+1) L_y)^2 \right)^{-1/2} \tag{18}$$

$$\xi_{ij,N_{im}} = \tfrac{1}{2} \left(\int_{N_{im}}^{\infty} \left(A_{ij,n}^- + A_{ij,-n} - A_{ij,n} - A_{ij,-n} \right) \mathrm{d}n + \right.$$
$$\left. \int_{N_{im}+1}^{\infty} \left(A_{ij,n}^- + A_{ij,-n} - A_{ij,n} - A_{ij,-n} \right) \mathrm{d}n \right) \tag{19}$$

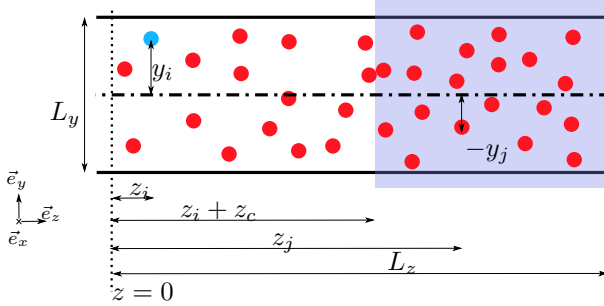$$r_{ij} = \sqrt{(x_i - x_j)^2 + (z_i - z_j)^3} \tag{20}$$

Fig. 1 – The cumulative influence of all particles beyond the axial position $z_i + z_c$ on the blue particle at (y_i, z_i) is sufficiently small to be neglected.

B. Electrostatic interaction

As the particles acquire charge they exert a electrostatic force on each other. This is described by Eq. (17) where also the influence of the conducting walls are taken into account using the methods of images. It should be noted that only the two walls at $y = \pm L_y/2$ are considered conductive, the other two walls (at $x = \pm L_x/2$) are considered electrostatically inert. This is done for two reasons. First this reduces the number of images and thus the number particle-image interactions and thus computational time. Furthermore, for the case of two parallel plates an analytical approximation for the far field potential is derived by Pumplin et al. [16]; this can supersede the method of images to calculate the potential field of a particle, if it is further than some critical distance z_{ff} away. We chose $z_{ff} = 1.5L_y$ because test calculations revealed that this approximation is always within 10% accuracy for $z_{ij} > 1.5L_y$.

By using the method of images, an infinite sum of interaction need to be calculated, because every image in one plate, has an image in the other. This sum can be approximated by a finite sum plus residual $\xi_{ij,N_{im}}$ if the sum is monotonously decreasing. This is the case if the denominator of $A_{ij,n}^+$ and $A_{ij,n}^-$ (Eq. (18)) is larger than zero for all n between N_{im} and ∞. Because $z < z_{ff}$ and $-L_y/2 < y_i, y_j < L_y/2$ this enforces a minimum number of images that need to be taken into account. For our choice of z_{ff} and L_y this means two images or more.

Because the electrostatic potential decreases with increasing interparticle distance, their interaction can be neglected if the distance is further than some cut-off distance z_c. However, note that this is only true if the cumulative influence of all particles beyond z_c is smaller than some threshold. This is graphically represented in Fig. 1.

This cumulative force can be calculated using the far-field approximation from Equation 17 for $z > z_{ff}$, assuming a homogeneous particle distribution. When this is less than 1% of the gravitational force on the particle, we consider it negligible. This leads to a cut-off distance in the range $2L_y \leq z_c \leq 3L_y$ for the applied saturation charge density and range of particle volume fractions. Because the domain is very long, $L_y \ll L_z$ this greatly enhances the efficiency of the simulation.

C. Charging model

Due to the tribo-electric effect, particles will charge when they collide with the wall. As we are in the state of building a learning model, we are at the moment not interested in a very accurate charging model. It must serve the purpose of revealing the importance of taking into account the image charges.

To that end, we assume that a particle will acquire its saturation charge density, σ_{sat}, over an area equal to the effective contact surface area A_c^*. In that case, the acquired charge of the particle equals

$$\Delta q = \sigma_{sat} A_c^*. \tag{21}$$

For consecutive particle-wall collisions, the contact surface area can overlap with the surface charged in the previous collisions; that part of the surface should not acquire any extra charge. To account for this, the part of the surface that makes contact for the first time, A_c^*, is estimated using the first order estimation

$$A_c^* = \alpha A_c \left(1 - \frac{A_{charged}}{A_p}\right), \tag{22}$$

where $A_{charged}$ is the surface area charged in previous collisions, A_p the total particle surface area and A_c the contact surface area. Consequence of the model, is that the saturation charge of the particle is given by

$$q_{sat} = \sigma_{sat} A_p. \tag{23}$$

The value for A_c is estimated using Hertz contact theory [17], assuming that the kinetic energy will be completely transfered to elastic energy. In that case

$$A_c = \pi \left(\frac{5 m_{ij} R_{p,ij}^2}{4 E_{ij}}\right)^{2/5} v_n^{4/5}. \tag{24}$$

with v_n the normal impact velocity and

$$\frac{1}{m_{ij}} = \frac{1}{m_i} + \frac{1}{m_j} \quad , \quad \frac{1}{R_{p,ij}} = \frac{1}{R_{p,i}} + \frac{1}{R_{p,j}} \quad \text{and} \quad E_{ij} = \frac{4}{3} \frac{1}{\frac{1-\nu_i^2}{E_i} + \frac{1-\nu_j^2}{E_j}}, \tag{25}$$

where the subscripts refer to particle (or wall) i and j that collide, and m, R_p, E and ν to their mass, radius, elastic modulus and Poisson ratio respectively.

α can be viewed of as a parameter that governs the charging efficiency and will change the amount of charge particles will attain when moving through the duct. A physical interpretation of α can be found in the increase of effective contact surface area due to rolling and sliding, as this is not taken into account in the Hertz contact model. Nevertheless, α is above all a simulation design parameter to enable the investigation of charging behavior on particle distribution without the need to be concerned about the actual physical material.

TABLE III – Overview simulation parameters.

Quantity	value	dimension
D_p	$60 \cdot 10^{-6}$	m
$\bar{v}_{bg}$	10	$m\,s^{-1}$
L_x, L_y	$2 \cdot 10^{-3}$	m
L_z	$2 \cdot 10^{-2}$	m
N_x, N_y	10	-
N_z	500	-
Δt_{DEM}	10^{-7}	s
Δt_{CFD}	$1.5 \cdot 10^{-5}$	s
t_{sim}	0.2	s
σ_{sat}	$2.7 \cdot 10^{-5}$	m
ν_{wall}, ν_p	0.35	$-$
E_p	$3 \cdot 10^9$	Pa
E_{wall}	$69 \cdot 10^9$	Pa
N_p	10^4	-
$e_{p \to p}$	0.97	-
$e_{p \to w}$	0.85	-
$\beta_{p \to p}$	0.46	-
$\beta_{p \to w}$	0.55	-
$\mu_{p \to p}, \mu_{p \to w}$	0.189	-
ρ_p	1050	$kg\,m^{-3}$
ρ_g	1.29	$kg\,m^{-3}$
η_g	$1.8 \cdot 10^{-5}$	$Pa\,s^{-1}$

D. Simulation setting

The simulation parameters are summarized in Table III. The particles are introduced at a random (x, y)-position at $z = 0$. Their z-velocity is equal to the local gas velocity $u_{g,z}(x, y)$, with random motion added, drawn from a Rayleigh distribution with scale parameter $u_{g,z}(x, y)/10$. Their x- and y-components of the velocity are drawn from a Gaussian distribution around zero, with standard deviation $u_{g,z}(x, y)/10$.

To investigate the influence of the image charges on the particles trajectory for a given charge per tube volume, we simulated at different mass flow rates (10 and 100 $mg\,s^{-1}$) and different values of α (10, 30, 100 and 300).

III. RESULTS AND DISCUSSION

To show the influence of the image charges the Probability Density Functions (PDF's) of the charge of a particle and the y position of a particle has been plotted for two different mass flow rates, $\dot{m} = 10mg\,s^{-1}$ and $\dot{m} = 100mg\,s^{-1}$, in Fig. 2 and Fig. 3, respectively. In all cases, the PDF of the charge per particle depends on the charging efficiency α.

For the lower mass flow rate without image charges (Fig. 2 top left) almost all particles acquire a minimal charge for $\alpha = 10$. With increasing α the distribution flattens, with a small peak at the saturation charge ($q = 3.05 \cdot 10^{-13}\,C$) for $\alpha = 300$. Something similar is seen when the same simulation is run with inclusion of image charge interaction(Fig. 2 top right). The main difference is that for $\alpha = 100$ and 300, many more particles attain the saturation charge.
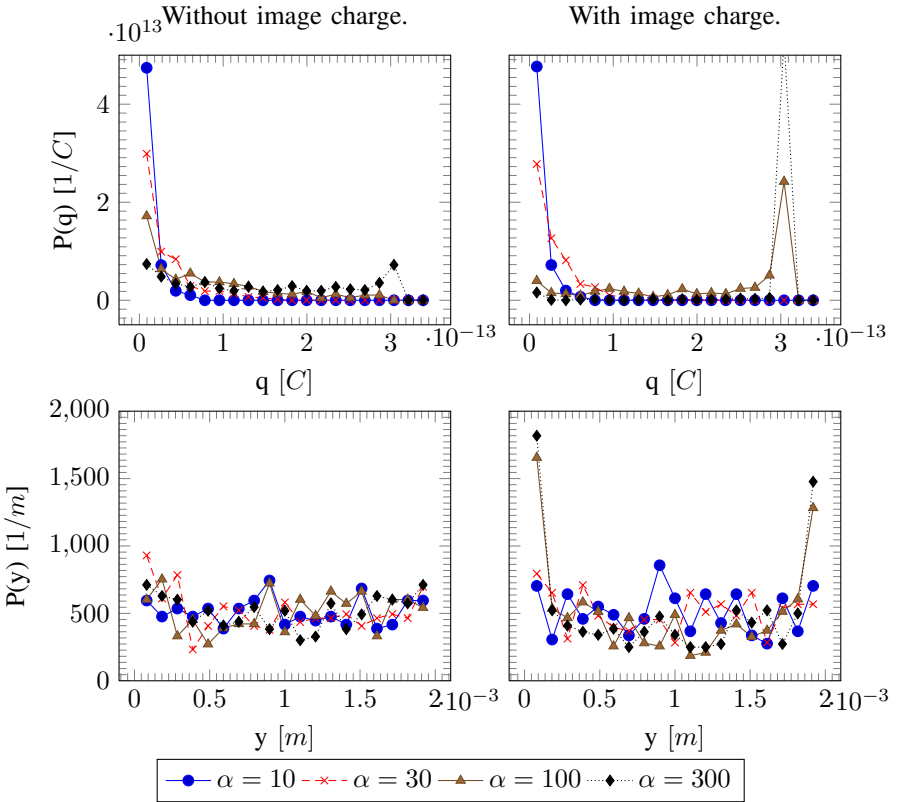
Fig. 2 – The probability density function (PDF) of the charge per particle (upper row) and the particles' position in y-direction (lower row) for simulations without (left column) and with (right column) taking image charges into account. In each plot the result for different α (Eq. (22)) is given, where the value of α is given in the legend. The mass flow rate is $10\,mg\,s^{-1}$. Note how the particles tend to reside closer to the wall ($y = 0$ and $y = 0.002$) for $\alpha = 100$ and 300 when images are taken into account (right). In all other cases the particles have equal probability to reside at any y-position.

When examining the spatial distribution of the particles in y-direction without image charges (Fig. 2 bottom left), there seems to be no preferred position as the distribution function is flat for all α's. For the simulation with images (Fig. 2 bottom right) this also holds when α is set to 10 or 30. However, when it is set to 100 or 300, the particles have a strong tendency to reside near the wall ($y = 0$ or $y = 2 \cdot 10^{-3}$).

For the higher mass flow rate without image charges (Fig. 3 top left), the behavior of the PDF of the charge per particle is similar to the one from the low mass flow rate simulation: for low α most particles have low charge, for increasing α the distribution transforms to higher charge and for the highest α most particles have the saturation charge. However, the mean charge is higher compared to the mean charge at lower mass flow rate for $\alpha = 30$, 100 and 300.
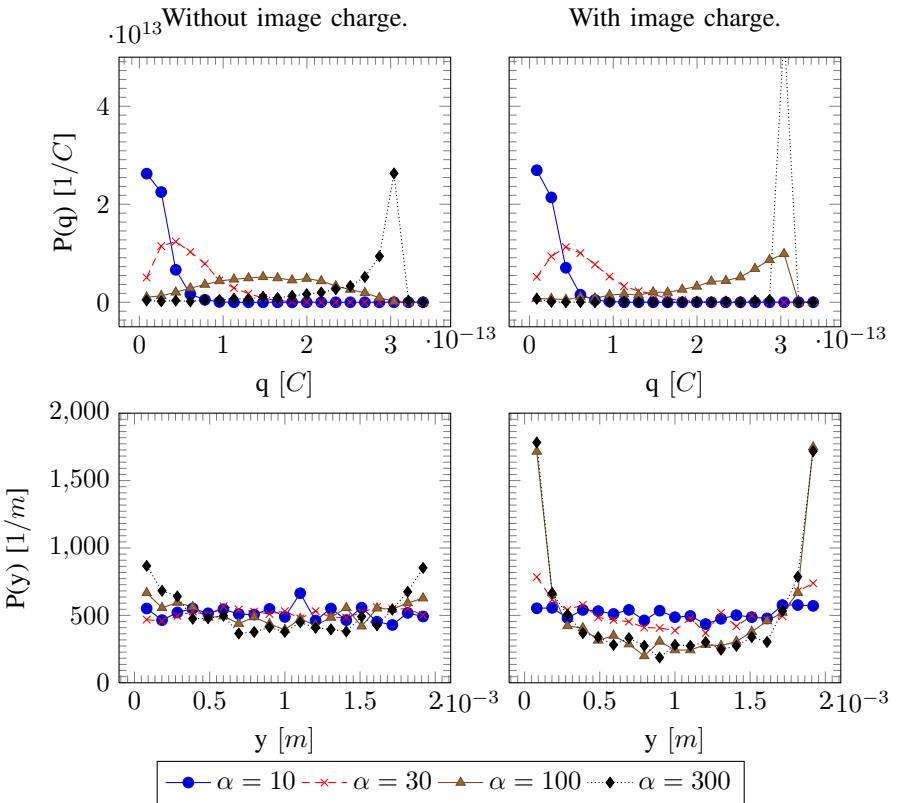
Fig. 3 – The probability density function (PDF) of the charge per particle (upper row) and the particles' position in y-direction (lower row) for simulations without (left column) and with (right column) taking image charges into account. In each plot the result for different α (Eq. (22)) is shown, where the values of α are given in the legend. The mass flow rate is $100\,mg\,s^{-1}$. Note how the particles tend to reside closer to the wall ($y = 0$ and $y = 0.002$) for $\alpha = 100$ and 300 without taking images into account (left). The same is also seen when images are taking into account (right), where the effect is much stronger and already visible for $\alpha = 30$.

When the simulation is repeated with image charges (Fig. 3 top right), a similar behavior is obtained. However, the mean charge per particle increases. This was also seen for the lower mass flow rate except for the lower peak at the saturation charge and the wider spread of the spatial distribution for $\alpha = 100$.

The PDF of the spatial particle distribution without images, (Fig. 3 bottom left), shows an equal probability on any y-position for $\alpha = 10$ or 30. For $\alpha = 100$ or 300 an increasing tendency to reside near the wall is seen. Note that this was not observed for the lower mass flow rate.

When including the image forces (Fig. 3 bottom right), the spatial distribution for $\alpha = 10$ remains the same, while for $\alpha = 30$ particles are more likely to reside near
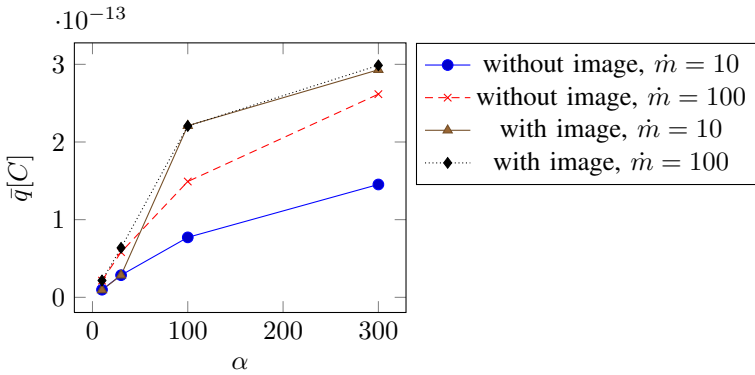
Fig. 4 – The mean charge per particle as function of different alpha is shown for a mass flow rate of 10 and 100 $mg\,s^{-1}$. These are from the simulation with image charges taken into account.

the wall. For $\alpha = 100$ and 300, the particles are much more likely to be near the wall. This influence of the images is the same as for the low mass flow rate, except that the influence is already observed at a lower charging efficiency ($\alpha = 30$ instead of 100).

These simulations show that if the charging efficiency α is sufficiently high, the image charges have a strong effect on both the positions and charges of the particles. This is effect is stronger at a higher mass flow rate. It should be noted that also without images, the particles have an increased mean charge with increased mass flow rate. It is therefore interesting to see whether increased charge per particle, or the increased volumetric charge density inside the tube is the reason for this behavior.

We observed that the volumetric charge density for the low mass flow rate with $\alpha = 100$ is equal to the charge density of the high mass flow rate with $\alpha = 10$. This suggests that the volumetric charge density is not the determining factor, because a strong influence of images is seen for the first case, while no influence of images is seen for the latter.

Another determining factor may be the mean charge per particle. Note that the influence of images start to show for the low mass flow rate (Fig. 2) when α is somewhere between 30 and 100, while for the high mass flow rate (Fig. 3) this critical α is around 30. In Fig. 4 the mean charge per particle is shown as function of α. If there is a critical mean charge per particle it should lie between the mean of the low mass flow rate of $\alpha = 30$ and 100 and around the mean charge per particle for the high mass flow rate for $\alpha = 30$. Indeed this last value ($\bar{q} = 6.3 \cdot 10^{-14}\,C$, lies between the first two, $\bar{q} = 0.94 \cdot 10^{-14}$ and $\bar{q} = 2.21 \cdot 10^{-13}\,C$. Once the charge exceeds this 'critical point' the charge will increase even more if images are taken into account. This is caused by the fact that a particle will be trapped at the wall if it does not have enough kinetic energy to escape the attraction of its image charge. In this case, the particle will hit the wall more and more and thus attaining extra charge which will make it even harder to escape. Hence, this can be considered a feed forward loop.

A naive estimate of this critical charge can be derived by assuming that the kinetic

energy E_{kin} of the velocity component normal to the wall v_n is completely transferred to electric energy at the point where the particle touches the wall. We neglect drag and the attraction of the image by the opposite wall. This yields the following balance

$$E_{kin} = \Phi_{wall} \tag{26}$$

$$\frac{1}{2}\rho\frac{4}{3}\pi R_p^2 v_n^2 = \frac{q^2}{4\pi\varepsilon_0}\frac{1}{2R_p} \tag{27}$$

$$q = \sqrt{\frac{16}{3}\varepsilon_0\rho\pi^2 R_p^4 v_n^2} = 6.14 \cdot 10^{-13} \tag{28}$$

with typical simulation parameters $\varepsilon_0 = 8.85 \cdot 10^{-12}\ Fa\,m-1$, $\rho = 10^3\ kg\,m^{-3}$, $R_p = 30 \cdot 10^{-6}\ m$, $L_y = 2 \cdot 10^{-3}\ m$, $v_n = 1\ m\,s^{-1}$. This estimate of the critical charge is one order of magnitude higher than $6.3 \cdot 10^{-14}$ which we derived from Fig. 4. It is also higher than the saturation charge. This suggests that only the interaction between the particle and its own image is not sufficient to estimate the importance of image charges. The interaction between all other particles and their images might need to be taken into account.

Note the rise of the mean charge per particle when increasing the particle mass flow rate. We do not have an explanation for this at the moment, but it will be topic of our next paper.

Finally, one should note the tendency of particles to reside close to the wall for the high mass flow rate with $\alpha = 100$ and $\alpha = 300$ even when *no* images are taken into account. This cannot be explained by the attraction of induced charges at the wall, because it is not modeled. It can be explained from the fact that equally charged particles repel each other and the imbalance of such forces near a wall. Consequently, particles have a higher likelihood to be near the wall. This effect however, is orders of magnitude smaller than the attraction by image charges and therefore only visible for denser particle flows with high charge per particle.

TABLE IV – List of Symbols.

Symbol	Quantity	Dimension
C_D	Drag coefficient	-
D_p	Particle diameter	m
E_{wall}, E_p	Youngs modulus of wall and particle	Pa
$\vec{e}_n, \vec{e}_t$	Normal and tangential unit vector of two colliding particles	-
$e_{p\to w}, e_{p\to p}$	Coefficient of normal restitution between wall/particle	-
g	Gravitational acceleration	$m\,s^{-2}$
k_n, k_t	Normal and tangential particle spring stiffness	$N\,m^{-1}$
L_x, L_y, L_z	x, y, z-dimensions of duct	m
$\dot{m}$	Particle mass flow rate	$mg\,s^{-1}$
m_p	Particle mass	kg
N_c	Number of contacting particles	-
N_c, N_p	Number of particles inside domain	-
N_{im}	Number of image charges	-
N_x, N_y, N_z	Number of computational cells flow solver, in x, y, z-direction	-
p	Gas pressure	Pa
q, q_{sat}	Charge and saturation charge on particle	C
q_{in}	Charge on particle before impact	C
r_{ij}	Distance between particle i and j perpendicular to duct axis	m
Re_p	Particle Reynolds number	-
t_{sim}	Total simulation time	s
V_p	Particle volume	m^3
$\bar{v}_{bg}$	Mean background gas velocity	$m\,s^{-1}$
$\vec{v}_p, \vec{v}_g$	Velocity vector of particle and gas	$m\,s^{-1}$
z_{ff}, z_c	Electric far field and cut-off distance along duct axis	m
z_{ij}	Distance between particle i and j along duct axis	m
α	Charging efficiency	-
$\beta_{p\to w}, \beta_{p\to p}$	Coefficient of tangential restitution between wall/particle	-
$\Delta t_{DEM}, \Delta t_{CFD}$	DEM and flowsolver timestep size	s
Δq	Acquired charge on impact	C
δ_n, δ_t	Normal and tangential overlap of colliding particles	m^{-1}
ε	Gas volume fraction	-
ε_0	Permetivity of vacuum *or* electric constant	$Fa\,m^{-1}$
η_n, η_t	Normal and tangential damping coefficient	$Ns\,m^{-1}$
μ	Friction coefficient of particle	-
μ_g	viscosity of gas	$Pa\,s^{-1}$
$\mu_{p\to p}, \mu_{p\to w}$	Coefficient of friction between wall/particle	-
ν_{wall}, ν_p	Poisson ratio of wall and particle	$-$
$\xi_{ij,N_{im}}$	Residual of sum trunctacted at N_{im}	m^{-1}
ρ_p, ρ_g	Density of particle respectively gas	$kg\,m^{-3}$
σ_{sat}	Saturation charge density	$C\,m^{-2}$
Φ	Electric potential	J

IV. CONCLUSION

We have shown that image charges can play a significant role in the spatial distribution of particles, as well as their acquired charge. However, if the charge on particles is low enough, their interaction with the induced charge may be neglected. As this is influenced by e.g. the mass flow rate, this decision is hard to make a priori and therefore care should be taken when neglecting them.

Furthermore, our results show that it is delicate to decide when a charge is sufficiently low: a small increase (three fold) in mean charge had a high influence on the particles' charge and spatial distribution.

V. OUTLOOK

In our future work we will increase our parameter space to determine the relevant parameters in this model. For example the inlet conditions and details of the gas flow. A sub-grid turbulence model will be added to enable simulations at higher (duct) Reynolds numbers. Furthermore, the charging model will be improved by adding the influence of space charge and a more detailed estimation of contact area by including rolling and sliding of the particles.

On the validation part, Particle Image Velocimetry (PIV) measurements are planned in combination with Digital Image Analysis (DIA). This will be used to investigate the distribution of particles' velocity and position in an experimental set-up. The experimental set-up has a geometry and configuration similar to our model. We will furthermore compare the experimentally determined charge per mass of the particles to the predictions of our DEM-CFD model. The ultimate goal will be to have a predictive model for the charge per particle in charging tubes employed for dry-fractionation.

VI. ACKNOWLEDGMENTS

REFERENCES

[1] M. A. I. Schutyser and A. J. v. d. Goot, "The potential of dry fractionation processes for sustainable plant protein production," *Trends in Food Science & Technology*, vol. 22, no. 4, pp. 154–164, 2011.

[2] P. J. Pelgrom, A. M. Vissers, R. M. Boom, and M. A. Schutyser, "Dry fractionation for production of functional pea protein concentrates," *Food Research International*, 2013.

[3] G. Wu, J. Li, and Z. Xu, "Triboelectrostatic separation for granular plastic waste recycling: A review," *Waste Management*, vol. 33, no. 3, pp. 585–597, 2013.

[4] S. Matsusaka, H. Maruyama, T. Matsuyama, and M. Ghadiri, "Triboelectric charging of powders: A review," *Chemical Engineering Science*, vol. 65, no. 22, pp. 5781–5807, 2010.

[5] T. Matsuyama and H. Yamamoto, "Charge relaxation process dominates contact charging of a particle in atmospheric conditions," *Journal of Physics D: Applied Physics*, vol. 28, p. 2418, 1995.

[6] T. Matsuyama and H. Yamamoto, "Characterizing the electrostatic charging of polymer particles by impact charging experiments," *Advanced Powder Technology*, vol. 6, no. 3, pp. 211–220, 1995.

[7] K.-i. Tanoue, H. Tanaka, H. Kitano, and H. Masuda, "Numerical simulation of tribo-electrification of particles in a gas–solids two-phase flow," *Powder Technology*, vol. 118, no. 1–2, pp. 121–129, 2001.

[8] M. D. Hogue, C. I. Calle, P. S. Weitzman, and D. R. Curry, "Calculating the trajectories of triboelectrically charged particles using discrete element modeling (dem)," *Journal of Electrostatics*, vol. 66, no. 1, pp. 32–38, 2008.

[9] M. D. Hogue, C. I. Calle, D. R. Curry, and P. S. Weitzman, "Discrete element modeling (dem) of triboelectrically charged particles: Revised experiments," *Journal of Electrostatics*, vol. 67, no. 4, pp. 691–694, 2009.

[10] T. Matsuyama, E. Šupuk, H. Ahmadian, A. Hassanpour, and M. Ghadiri, "Analysis of tribo-electric charging of spherical beads using distinct element method," vol. 1145, pp. 127–130, 2009. cited By (since 1996) 0.

[11] P. M. Ireland, "Triboelectrification of particulate flows on surfaces: Part ii mechanisms and models," *Powder Technology*, vol. 198, no. 2, pp. 199–210, 2010.

[12] M. Van der Hoef, M. Ye, M. van Sint Annaland, A. Andrews, S. Sundaresan, and J. Kuipers, "Multiscale modeling of gas-fluidized beds," vol. 31, pp. 65–149, 2006.

[13] T. B. Anderson and R. Jackson, "Fluid mechanical description of fluidized beds. equations of motion," *Industrial & Engineering Chemistry Fundamentals*, vol. 6, no. 4, pp. 527–539, 1967.

[14] P. A. Cundall and O. D. Strack, "A discrete numerical model for granular assemblies," *Geotechnique*, vol. 29, no. 1, pp. 47–65, 1979.

[15] M. A. Van der Hoef, M. van Sint Annaland, N. G. Deen, and J. A. M. Kuipers, "Numerical simulation of dense gas-solid fluidized beds: A multiscale modeling strategy," *Annu. Rev. Fluid Mech.*, vol. 40, pp. 47–70, 2008.

[16] J. Pumplin, "Application of sommerfeld-watson transformation to an electrostatics problem," *American Journal of Physics*, vol. 37, p. 737, 1969.

[17] K. L. Johnson, *Contact mechanics*. Cambridge university press, 1987.